High-throughput experimentation for microstructural design in additively manufactured 316L stainless steel

Ankur Kumar Agrawal[1,2], Gabriel Meric de Bellefon[1,2], Dan Thoma[1, 2]
[1]Department of Materials Science and Engineering, UW-Madison, Madison 53706, USA
[2]Grainger Institute for Engineering, UW-Madison, Madison 53706, USA

Abstract:
In the present study, a combination of high-throughput (HT) and low-throughput (LT) techniques was used to rapidly determine the processing window and generate processing maps for Selective Laser Melting (SLM) of 316L stainless steel. The HT method includes the fabrication of hundreds of hex nut-shaped specimens, each processed with a unique combination of laser power, scanning speed, and hatch spacing. An easily removable scaffolding permitted rapid sample extraction from the base plate, thus saving machining cost and time. Hardness and immersion density measurements were used for HT characterization to identify a processing window for maximum strength and density. Within the defined processing window, a low-throughput (LT) microstructural interrogation of specimens were performed. The microstructural analysis included quantification at various length scales (i.e., grains size and morphology, texture, primary dendrite arm spacing, and melt pool geometry analysis). Microstructure-based processing maps as a function of volumetric energy density were generated. The combination of HT and LT methods produced a predictive relationship between hardness and primary dendrite arm spacing using a Hall-Petch relationship. A model is proposed to explain the dependence of microstructure on the melt pool geometry. The HT method can be applied for the microstructural design of SLM-fabricated components in other alloys.

Keywords:
Additive manufacturing, Selective Laser Melting, 316L stainless steel, High-throughput experiments, Processing maps

Corresponding Author:
Prof. Dan Thoma (dthoma@wisc.edu)
M1080, Engineering Centers Building, 1550 Engineering Drive, Madison, WI 53706-1691

1. Introduction

1.1 Challenges and Opportunities in Additive Manufacturing

Additive manufacturing (AM) is a process to fabricate components through the layer-by-layer deposition of materials. Examples of metal powder AM techniques include selective laser melting (SLM), directed energy deposition (DED), and electron beam melting (EBM) [1]. The underlying principle behind these processes is to introduce material in powder or wire form and melt them using a high energy source such as a laser or electron beam. Over the past decade, the SLM process has gained high interest especially among energy, defense, and aerospace industries [2]. The SLM process enables the printing of complex geometries with the potential for lower cost and minimizing material waste [2,3]. However, SLM parts often contain processing defects such as porosity, inclusions, residual stress, and anisotropic properties. The defect concentration, microstructure, and property anisotropy depend upon processing conditions such as laser power, scanning speed, hatch spacing, and layer thickness [1,2,4]. As a consequence of processing defects, qualification and certification of fabricated parts can be challenging [5] and limit the use of metal AM parts. To fully exploit the SLM process, it is necessary to design, predict, and control the microstructural development in viable processing ranges.

Processing ranges in SLM are bounded by the challenge to fabricate a defect-free, fully dense component. Many studies [6–9] have focused on pore characterization and how these defects form during AM processing. Pores due to localized lack-of-fusion are commonly observed in AM parts where insufficient input energy results in weak bonding between the layers [10]. In a study by Mukherjee *et al.* [11] a normalized heat-input parameter (non-dimensional number) showed a linear dependence with the amount of lack-of-fusion defects. Conversely, keyholing occurs due to excessively high energy input [12]. These solidification defects can lead to catastrophic failure. For example, failure analysis of additively manufactured 316L SS specimens showed the initiation of cracks at the fabrication-induced pores and defects during tensile testing [13]. In as-fabricated AM parts, defect morphologies, which can vary from spherical pores to high aspect ratio cracks, can also impact failure. For example, accelerated crack initiation was observed in the specimens having lack-of-fusion defects during a high-cycle fatigue testing, whereas a minimal effect was observed in specimens having small equiaxed pores [14].

Another challenge in the SLM process is the ability to predict and control the microstructure. Solidification microstructures are considered complex because of the moving localized heat source that overlaps with existing fusion tracks [5,15]. In addition, the moving heat source thermally affects prior layers as a function of spatial and temporal processing conditions. The solidification microstructural features depend mainly on the melt pool size and solidification conditions (i.e., thermal gradient (G) and solidification rate (R)) [6]. High thermal gradients and high cooling rates associated with the metal AM process result in the formation of microstructures consisting of high dislocations densities, low angle grain boundaries, sub-granular cellular structures, and crystallographic texture [4]. Microstructural analysis of SLM-fabricated 316L SS shows the presence of columnar grains and cellular-dendritic structures [16] with a cellular spacing increasing with the energy input [17]. Transmission Electron Microscopy (TEM) analyses of SLM 316L SS show the presence of dislocation networks in the cell boundaries region [4,18], which could be effective in blocking the motion of dislocations. In addition, epitaxial grain growth can occur multiple deposition layers, resulting in microstructures textured along the building direction. A study by Bertoli *et al*. [19] showed that crystallographic texture is strongly related to the melt pool geometry and hatch spacing.

When processing conditions are well selected, as-fabricated AM 316L SS can show higher strength and ductility as compared to wrought 316L SS [20]. The main factors attributed to a strength increase are the cellular dendritic structure, grain size, and dislocation density [18,21,22]. The increase in ductility was attributed to a higher propensity for deformation twinning [4,23,24]. AM 316L SS also showed excellent fatigue strength and fatigue crack growth threshold values as compared to wrought materials, primarily due to high yield strength to tensile strength ratios [25,26]. However, the columnar grain and crystallographic texture in the build direction can often lead to anisotropic properties. For example, in 304L SS higher ductility was observed along the transverse direction, as compared to building direction, while, both directions showed similar tensile strength [27].

1.2 High-Throughput Experiments in AM

Metal AM processing with SLM is controlled by at least 100 process variables [28]. Of these variables, laser speed, laser power, and hatch spacing are the more common and easily adjusted ones. Selecting the adapted variables for a given material, powder feedstock [29], and application can be challenging and time-consuming and often relies on trial and error.

High-throughput (HT) experiments may permit faster rates of design of experiments (DOE), particularly when guided with a fundamental premise [30,31]. Large datasets obtained from HT experiments can be used as training sets for various machine learning algorithms [32,33] and can be used to predict the process parameter ranges. Ren *et al.* [34] have demonstrated the combined use of HT and machine learning for the discovery of metallic glasses. Specifically, for AM, given a known set of process parameters corresponding to specific material, HT can allow a systematic interrogation of processing parameter variations. Moreover, the interdependence of the parameters can be developed to rapidly define correlations not available in existing models. Recent studies [35,36] using an automated HT tensile test were performed to evaluate the effects of processing parameters on the mechanical behavior of AM 316L SS. Other studies [37] have focused on HT process control via in-situ monitoring of the melt pool. To expand the AM techniques to other alloy systems, HT experiments are needed to quickly fabricate, characterize, and identify the appropriate processing window, especially since there are a large number of processing variables in the SLM technique.

Power-Velocity (PV) processing maps are a powerful way to visualize the effects of AM processing parameters on microstructure and performance. Processing maps for SLM techniques have been systematically used by Beuth *et al.* [38] where different regions of defects (i.e., lack-of-fusion and keyholing) were mapped at different laser power and scanning speed combinations. These maps provide useful information about the defect population and processing window to fabricate full density specimens. A few other recent studies [39,40] have also extended this idea and constructed processing maps for different alloy systems using experimental and computational techniques. Processing maps for welding, deformation, other manufacturing techniques were previously developed to guide users about the optimum processing conditions. However, most of these studies have focused on defects at different processing conditions, and there is a lack of understanding about microstructure evolutions at these conditions.

The novelty of the current work lies in using high-throughput fabrication and characterization techniques to quickly analyze SLM-fabricated 316L SS. These techniques allowed the identification of the processing bounds within a reasonable time frame of 2-3 days. Following the HT synthesis and characterization, low-throughput (LT) microstructural investigations on key specimens were performed to define the critical microstructural features and

to generate microstructure-based processing maps. This study will provide insights into the microstructural evolution and microstructural design strategies for SLM-fabricated parts. The new methodology can be applied to other alloy systems for rapid processing parameter discovery.

2. Experimental Procedure:

316L SS feedstock powder were procured from EOS GmbH, Germany. The powder particles were spherical in shape. The particle size range was 15-40 μm as provided by the supplier. The chemical composition of the powder as measured using plasma emission spectroscopy is shown in Table 1. Wrought 316L SS plates were used as the substrate material. Build plates were thoroughly cleaned using ethanol prior to fabrication.

Table 1. Chemical composition of the 316L SS powder

Elements	Fe	Ni	Cr	Mo	Si	Mn	C	N	Cu	P	O
wt. %	Bal	13.94	18.39	2.86	0.3	1.47	0.004	0.065	0.0022	0.0017	0.043

316L SS specimens were additively manufactured using the EOS M290 system. A 400 W Ytterbium fiber laser with a wavelength of 1060 nm and a beam diameter of 100 μm was used as the energy source. Build plates were preheated to 80˚C, and an inert argon atmosphere was maintained during the fabrication process. A set of hex nut-shaped specimens, each having a width of 3.17 mm (1/8th in.) and a height of 3.0 mm, was fabricated at different processing conditions. These specimens were deposited over a 3.0 mm porous support structure for easy removal from the build plate as shown in Figure 1. In the current study, the effects of the most influential parameters were studied, i.e., laser power (70-280 W), laser scanning speed (600-7000 m/s), and hatch spacing (0.07-0.36 mm). All the other processing parameters were kept constant such as layer height = 0.02 mm, build plate temperature = 80 ℃, stripe thickness = 5 mm, etc. The porous support structure was fabricated using the factory's default processing conditions. In addition, a volumetric energy density (VED) parameter was used to compare the combined effects of these parameters. VED (J/mm^3) signifies the amount of input energy into the melt pool and is defined by the equation:

$$VED = \frac{l_p}{v_s \times h \times t} \quad \text{(Eq. 1)}$$

where l_p is laser power (W), v_s is laser scanning speed (mm/s), h is hatch spacing (mm), and t is nominal layer thickness (mm).

The hex nut sample morphology developed for this investigation offered three advantages for a HT synthesis and evaluation. First, the specimens were quickly removed with a socket wrench. Next, removing the specimens by applying a torque resulted in minimal residue support structure on the sample, thus requiring no additional machining. Finally, the hex nut's flat surface permitted HT hardness investigations. A total of 425 hex nut specimens covering a wide range of VED (5-160 J/mm^3) were fabricated.

HT hardness and density measurements on all 425 hex nut specimens were performed. Hardness measurements were performed using the Rockwell A method, where a load of 60 Kgf was applied for a dwell time of 15 s. All the indents were made on the center of the side surface (xz plane) to maintain consistency. At least five indents were made on each specimen (as-fabricated surface) to get the average hardness measurements. An immersion density measurement method was used based on the Archimedes principle [41] using a Fluorinert™ FC-40 solution (density= 1.86 g/cc). An ASTM Standard B962 [42] was followed while measuring the density.

The relative density (%) was calculated with respect to wrought 316L SS alloy (density = 8.0 g/cm^3) [43]. Specimens with the highest density and hardness values were chosen for LT detailed microstructural characterization.

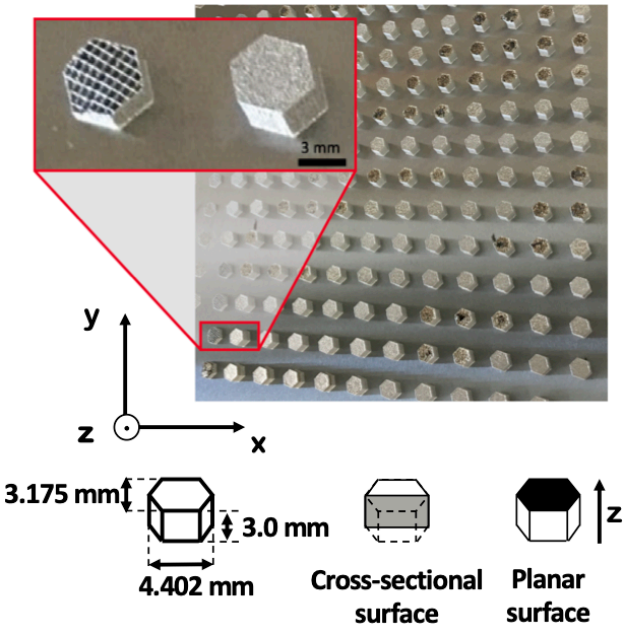

Figure 1 Schematic diagram of the hex nut geometry and a picture of the 316L SS hex nuts fabricated at different power and velocity combinations using an EOS M290.

Based on the results of the HT study, seven LT specimens were selected, as detailed in 3.2.1. The seven specimens were sectioned along the build direction and cold mounted using an epoxy resin to study the planar and the cross-sectional surface (as defined in Fig. 1). Planar surfaces were ground to the approximate depth of 1 mm from the bottom surface, and this depth was uniform for all of the specimens. A conventional metallographic practice involving mechanical grinding and polishing was used to prepare these specimens for further analysis. Final polishing was performed using a 0.5-micron alumina and 0.05-micron colloidal silica solution. Prior to microscopy, specimens were cleaned and rinsed using isopropanol. Electron backscatter diffraction (EBSD) mapping of planar surfaces was carried out in a FEI Helios G4 High-Resolution FEG-SEM. An accelerating voltage of 30 kV and a current of 51 nA was used to collect EBSD data form the 1x1 mm region with a step size of 1 µm. EBSD data was analyzed using the MATLAB based MTex toolbox, in particular to calculate grain sizes and textures. To calculate a grain size, grain boundaries having a misorientation greater than 5 degrees were mapped. Smaller grains (i.e., total grain area <20 µm^2) were removed from the analysis. The grain size was calculated by measuring the largest distance (in pixels) within each grain. Non-weighted number average provided the average grain size value. For texture analysis, the 'odf1' function was used to calculate the orientations of each pixels. A reconstruction of these datasets using the 'plotIPDF' function was done to generate IPF maps with the build direction as a reference direction.

Similar metallographic preparation and electrochemical etching were performed for the cross-sectional surfaces. Electrochemical etching of the 316L SS was done using a 0.1 M oxalic acid solution operated at 5.5 mV to reveal grain boundaries and dendrites. Chemical etching using

ferric chloride solution was used (i.e., 5 g $FeCl_3$, 20 ml HCl, 80 ml ethanol) to reveal the melt pool boundaries. Optical microscopy (OM) and Scanning Electron Microscopy (SEM) of cross-sectional surfaces were carried out in a Keyence VHX-5000 and a ZEISS LEO 1530 FEG-SEM respectively. An accelerating voltage of 5 kV was used to collect the SEM images. SEM and optical image analysis were performed using ImageJ software, in particular for dendrite analysis.

3. RESULTS

3.1 High-throughput characterization

3.1.1 Density measurements

Immersion-based density measurements of the hex nut specimens as a function of VED are shown in Figure 2a. In the lower VED range of 5-70 J/mm^3, the density of the specimen increases from 75% to 98.5% with increasing VED. A linear dependence of density with energy density suggests the presence of lack-of-fusion type defects in these specimens [11]. In the VED range of 5-20 J/mm^3, few specimens showed relatively higher densities than the rest of the specimens. In these specimens, open pores were observed (Fig. 2a) suggesting misleading density measurements, and thus those data points were treated as outliers. The presence of open pores in the unfused specimens is probably due to extremely low laser power or very high scanning speed values. A saturation point in the density was observed at 70 J/mm^3 which might be related to the lack-of-fusion offset. In the VED range of 70-150 J/mm^3, a similar and constant density was observed. The maximum density recorded was 7.90 g/cc (i.e., 99% dense as compared to wrought 316L SS). The actual specimen density may have some deviation due to surface roughness effects.

3.1.2 Hardness measurements

Average hardness measurements of the hex nut specimens are shown in Fig. 2b. Similar to density, the specimen's hardness increases with VED before reaching a maximum value of 50.1 HRA. Both density and hardness measurement showed a peak in the similar VED value suggesting a lack-of-fusion offset to be around VED ≈ 70 J/mm^3. Almost all the specimens in the lower VED, i.e., below 20 J/mm^3, showed a negative hardness value. The negative value stems from the material being too soft for the HRA scale measurement. The HRA scale is effective in measuring the hardness between 112 to 513 HV and if hardness is below 112 HV, Rockwell B or F scale should be used. Since most of the specimens were in the range of the HRA scale, only the HRA scale was used for consistency. A drop in the hardness from 50.1 to 39.95 HRA was observed in the VED ranging from 70-150 J/mm^3. The observed linear relationship between hardness and VED was obtained within the processing regime of VED = 70-150 J/mm^3 can be expressed by:

$$HRA = 53.3 - 0.055 \times VED \quad \text{(Eq. 2)}$$

A p-value of 4.9×10^{-24} suggests the data to be statistically significant, despite an R-square value of 0.424. Above 150 J/mm^3, the average hardness values had increased scatter.

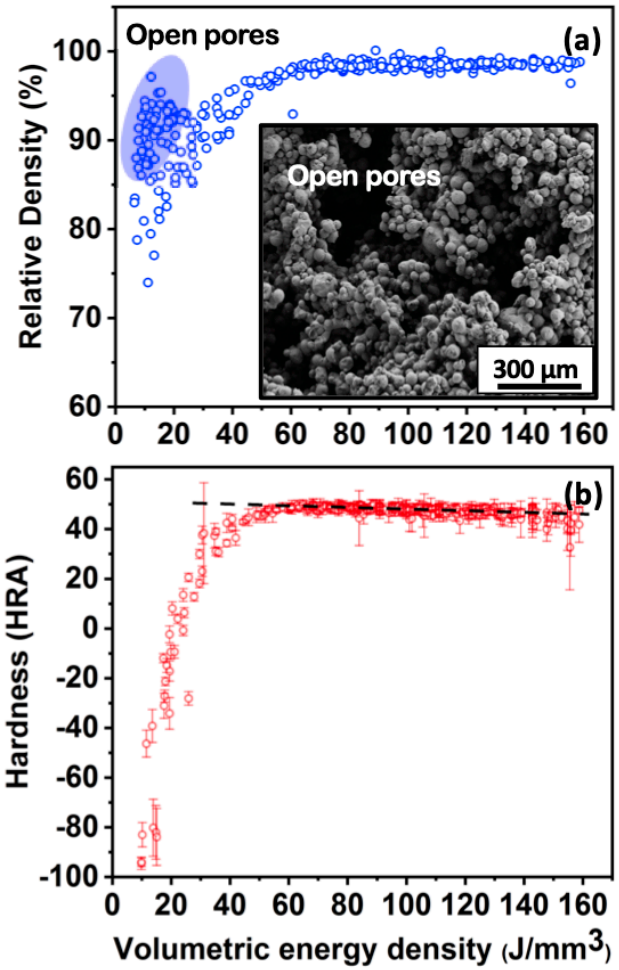

Figure 2 (a) High-throughput density measurement using Archimedes principle. Inset showing a SEM image of as-fab specimens (unpolished, bottom surface) having open pores. (b) High-throughput hardness measurement using a Rockwell indention.

3.1.3 *Defects and pores morphology*

SEM images of the defects and pores from different regions of the HT measurements are shown in Figure 3. At a very high energy density sample (VED = 212.1 J/mm^3) keyholing defects were observed (Fig. 3a). The keyholes were about 20-50 µm in size and had a spherical morphology. These defects were randomly distributed within the specimens and easy to find. The amount of keyhole pores was less prominent (but roughly the same size) as the VED approached 150 J/mm^3. Within the boundary regions of the LT study (i.e., VED = 70-150 J/mm^3) relatively dense specimens were obtained. These specimens (VED = 113.6 J/mm^3) showed pores in sub-micron size ranges (not clearly visible in Fig. 3b) and are potentially confused with inclusion pull-out. The specimens at lower energy density (VED = 41.9 J/mm^3) i.e., below the lower boundary region (< 70 J/mm^3) showed various characteristics of lack-of-fusion, processing cracks, and un-melted powders. (Fig. 3c). These defects have a high aspect ratio, and many have sharp edges. Overall, the defects and pores investigation showed a good correlation with the HT measurements.

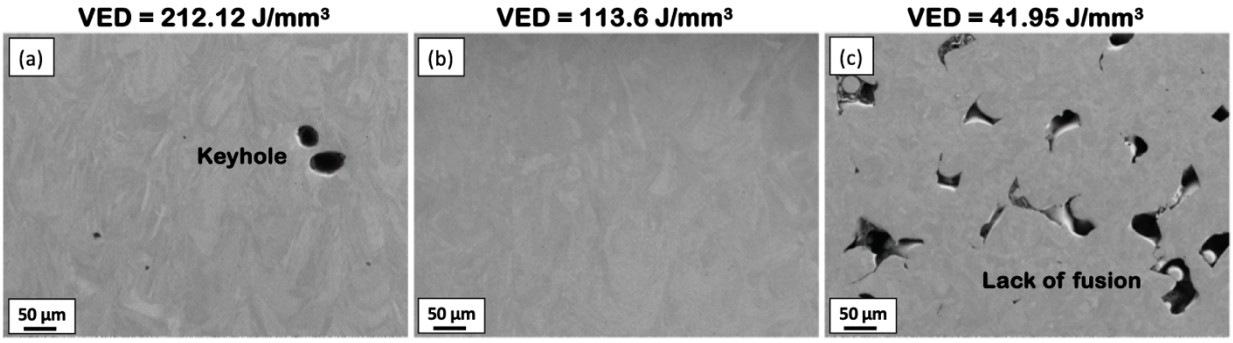

Figure 3 SEM images from different regions of PV maps showing (a) keyholes (b) high density and (c) lack-of-fusion type of porosities.

3.2 Low-throughput microstructural characterization

3.2.1 Specimens selection for low-throughput microstructural characterization

In the regime of constant density and hardness (i.e., VED = 70 J/mm^3 and 150 J/mm^3), seven specimens were selected for LT microstructural characterization as shown in Fig. 4a and b. All of the specimens were made using the same hatch spacing (0.11 mm) and the same layer thickness (0.02 mm), but different laser power and scanning speed listed in Table 2 and located in the PV maps in Fig 4c. All specimens were considered free of lack-of-fusion or keyholing defects, as the relative density was close to 99%.

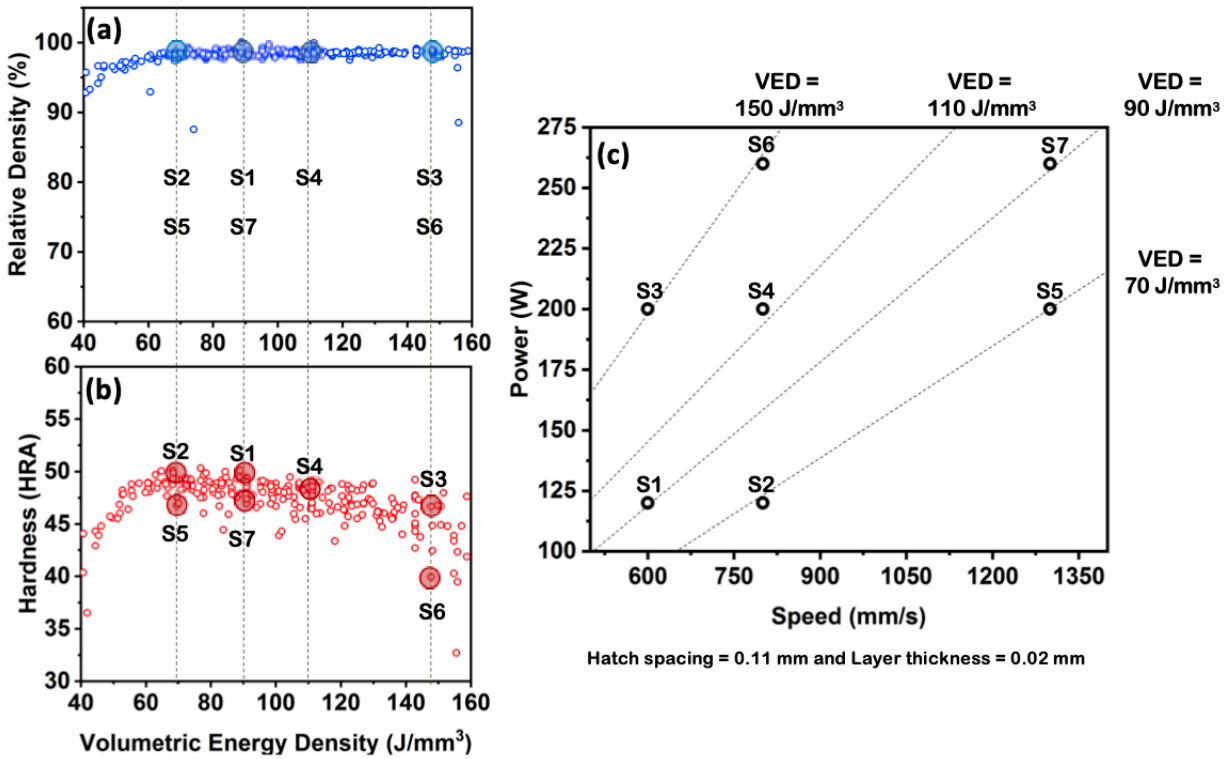

Figure 4 Specimens selection for low-throughput microstructural characterization.

Table 2. Processing parameters and LT characterization of the selected specimens

S.No.	Laser power(W)	Scanning speed (mm/s)	VED (J/mm^3)	Average grain size (μm)	Grain aspect ratios	Primary dendrite arm spacing (μm)
S1	120	600	90.9	26.13 ± 19.79	3.57± 1.23	0.42 ± 0.05
S2	120	800	68.2	22.82 ± 15.08	2.75± 1.41	0.40 ± 0.03
S3	200	600	151.5	35.07± 31.74	5.60± 2.51	0.56 ± 0.04
S4	200	800	113.6	34.33± 27.62	3.40± 1.90	0.46 ± 0.04
S5	200	1300	69.9	23.05± 16.31	2.98± 0.61	0.39 ± 0.03
S6	260	800	147.7	34.87± 33.64	4.97± 1.51	0.57 ± 0.10
S7	260	1300	90.9	30.94± 30.94	3.13± 1.44	0.47 ± 0.07

3.2.2 Average grain size and grain orientation

EBSD maps and inversed pole figure (IPF) plots of the S3, S4, and S5 specimen's planar surfaces are shown in Figure 5. From EBSD maps, it was observed that many grains had an irregular, elongated shape. In each specimen, the variation in grain size from 10 to 50 μm was observed. The average values of the grain size calculated from EBSD maps were compared among all seven specimens (see Table 2). As the energy density increases from 69.9 to 151.5 J/mm^3, an increase in average grain size from 23.05 to 35.07 μm was observed.

In addition, the texture of the specimens also varied with VED (Fig. 5). At a lower VED of 69.9 J/mm^3, a random texture was observed. With increasing VEDs, specimens showed a texture towards (110) and (100) plane with respect to the build direction (more green and red color grains). These specimens showed an IPF intensity of ≈2, which means twice the number of grains were oriented towards (110) plane than that of completely random texture. Also, in these specimens, none of the grains were oriented towards (111) plane. A similar variation in average grain size and texture with VED was observed for the rest of the specimens at different laser power (Table 2).

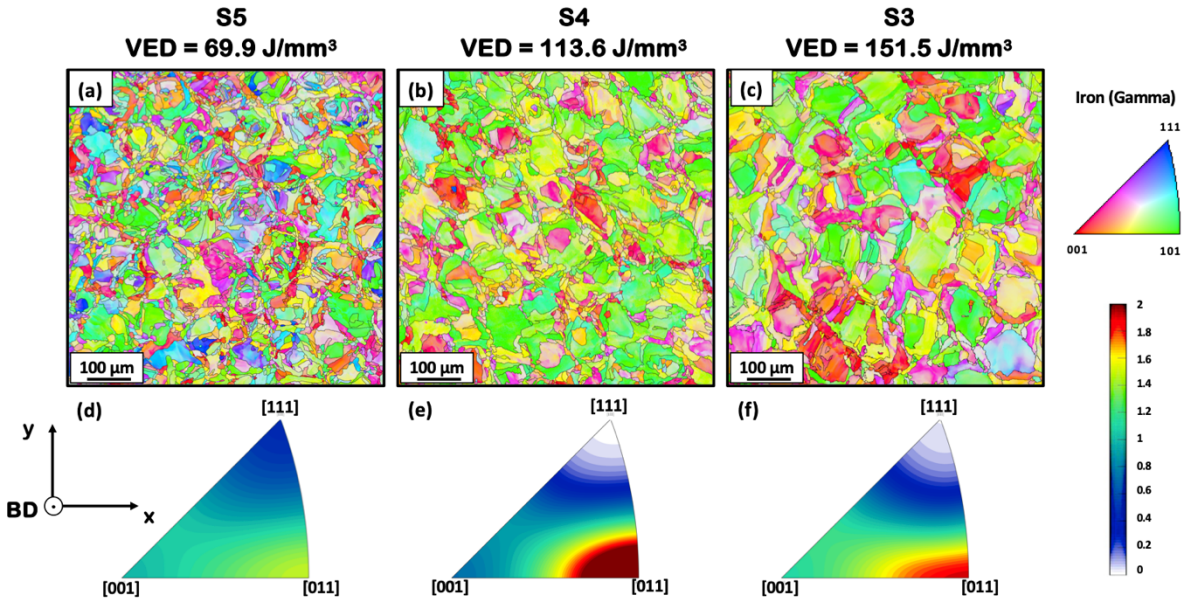

Figure 5 EBSD maps and IPF of the 316L SS SLM-fabricated specimens (a,d) S5, VED = 69.9 J/mm^3, (b,e) S4, VED = 113.6 J/mm^3, and (c,f) S3, VED = 151.5 J/mm^3. The reference direction for the IPF maps is Build direction (BD).

A similar microstructure was obtained at constant VED values. EBSD mapping of specimens S2 and S5 processed at similar VED ≈ 70 J/mm^3 are shown in Figure 6. In both specimens, the average grain size was measured to be 23.05 and 22.8 µm, and a random texture was observed. The difference in the average grain size was less than 5%. EBSD mapping of other specimens also showed similar average grain size values at constant VED of 90 J/mm^3 and 150 J/mm^3 (Table 2). Overall, these results suggest that the average grain size and the grain orientation depends upon the VED, and finer grains can be obtained at lower VED values.

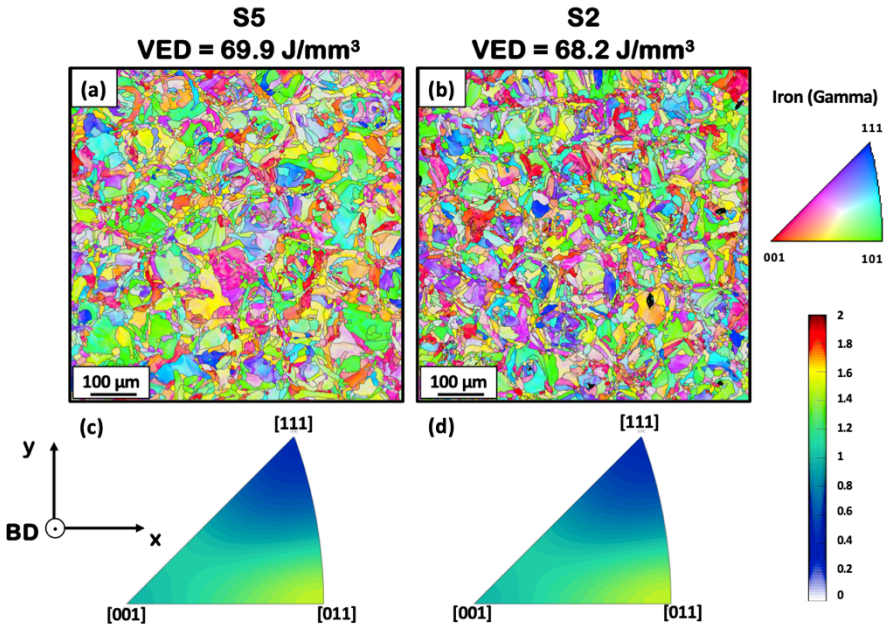

Figure 6 EBSD maps and IPF of the 316L SS SLM-fabricated specimens (a,c) S5, VED = 69.9 J/mm^3 and (b,d) S2, VED = 68.2 J/mm^3. The reference direction for the IPF maps is the Build direction (BD).

3.2.3 Grain morphology

The cross-sectional SEM images of the S3, S4, and S5 specimens are shown in Figure 7a-c. Specimens were aligned such that the build direction points upwards, and the SEM images were taken at a similar height in the build direction to maintain consistency. Grain boundaries (white boundaries) in each of the images were manually drawn. For each grain, longitudinal length and transverse length were measured. By analyzing multiple images from each processing condition, statistically, the average grain aspect ratio was calculated. At lower energy densities of 69.9 J/mm^3, more spherical grains were observed. The average grain aspect ratio was around 2.98 ± 0.61. As the energy density increased to 151.5 J/mm^3, the average grain aspect ratio also increased from 2.98 ± 0.61 to 5.16 ± 2.51. Interestingly, an increase in the average grain aspect ratio was accompanied by a simultaneous increase in both longitudinal length and transverse length. Qualitatively, both SEM analysis (cross-sectional surface) and EBSD analysis (planar surface) showed an increase in grain size with an increase in energy density.

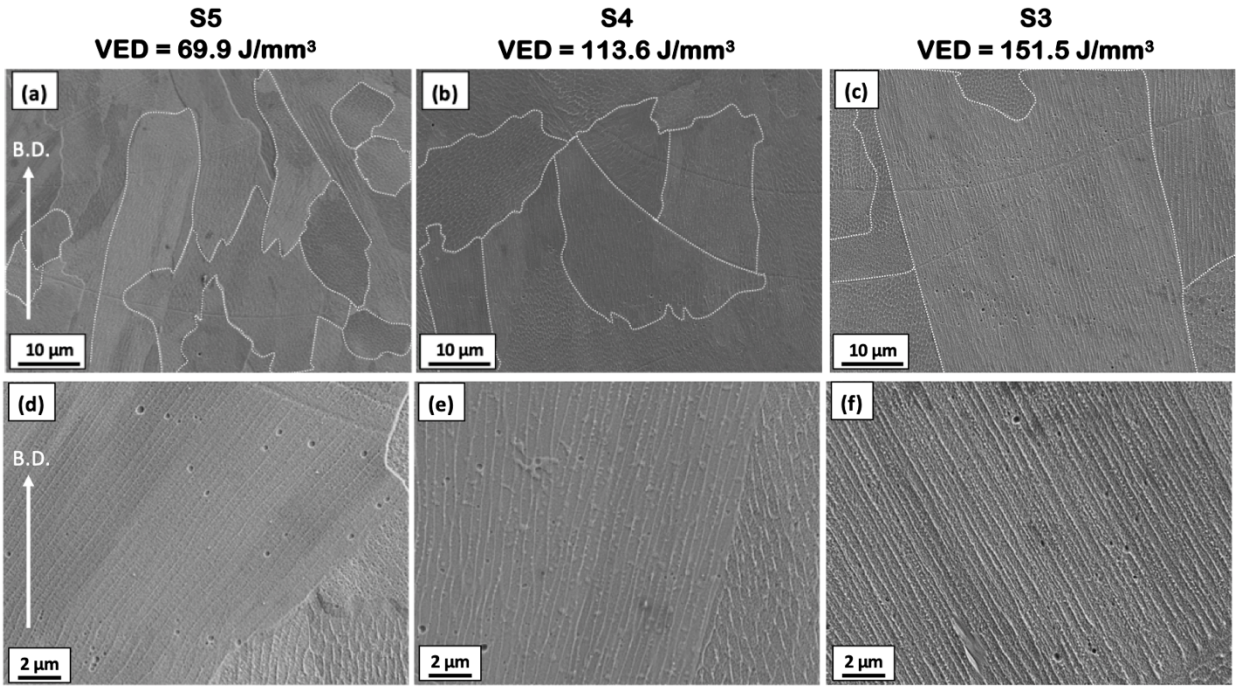

Figure 7 Cross sectional SEM images of the 316L SS SLM-fabricated specimens (a,d) S5, VED = 69.9 J/mm^3, (b,e) S4, VED = 113.6 J/mm^3, and (c,f) S3, VED = 151.5 J/mm^3 showing grain morphology (white dash lines) and primary dendrite arm spacing.

3.2.4 Primary dendrite arm spacing

The dendritic structure of the S3, S4, and S5 specimens is shown in Fig. 7d-f. In SLM components, the solidification structures vary along the z-direction owing to the variation in cooling rates. For comparison, specimens were aligned in the building direction and the various SEM images were captured at a similar z-height in each specimen. Also, images of dendrites were captured along the center of the melt pool to minimize the influences of heat affected zones. In each specimen, a similar dendritic morphology was observed suggesting similar solidification conditions at the solid-liquid interface. The distance between the dendrites was measured only for the cases in which the dendrites were long (the distance remains constant along the longitudinal direction) ensuring the dendrites were perpendicular to the surface. Multiple measurements (i.e., 15-20 per specimen) for primary dendrite arm spacing were performed. At lower energy densities of 69.9 J/mm^3, the average primary dendrite arm spacing measurement was 0.39 $\pm$ 0.03 µm. As the energy density increased to 151.5 J/mm^3, the average primary dendrite arm spacing increased by around 43% from 0.39 $\pm$ 0.03 µm to 0.56 $\pm$ 0.04 µm.

A linear relation between primary dendrite arm spacing and VED based on the regression analysis (R-square = 0.95, p-value = 1.9e-4) is shown in Figure 8. The equation to predict the PDAS (µm) in the VED regime of 70-150 J/mm^3 can be given by:

$$PDAS = 0.26 - 0.0019 \times VED \quad \text{(Eq. 3)}$$

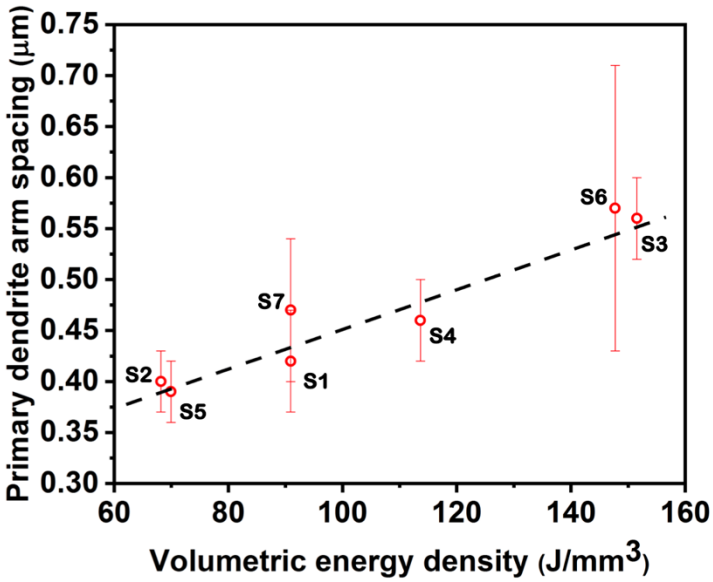

Figure 8 Regression analysis of primary dendrite arm spacing with volumetric energy density of the S1-S7 specimens.

3.2.5 Melt pool geometry

Melt pool boundaries of the S3, S4, and S5 specimens are shown in Figure 9. Successive overlapping of the melt pool is apparent in all of the specimens. The overlapping pools are essential for good bonding between the layers and fabricating fully dense components. Some of the layers have a long streak of the melt pool due to the orientation effects (hatch rotation of 67 degrees). A detailed measurement of the melt pool dimensions was difficult due to the orientation effects and the overlapping melt pools. The width and depth of some of the melt pool, especially at the top few layers, were easier to trace, and these values were used for analysis.

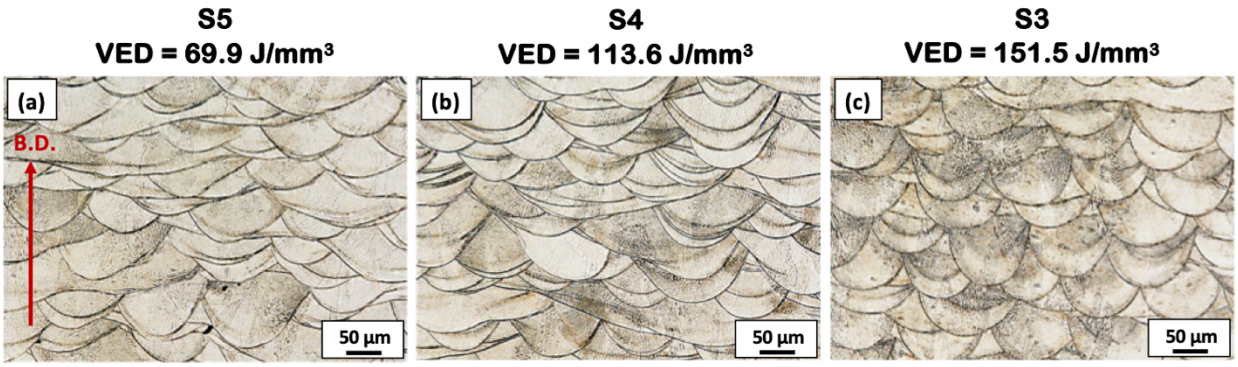

Figure 9 Cross sectional optical micrographs of the 316L SS SLM-fabricated specimens (a) S5, VED = 69.9 J/mm^3, (b) S4, VED = 113.6 J/mm^3, and (c) S3, VED = 151.5 J/mm^3 showing melt pool boundaries.

Dependence of the melt pool dimensions with energy density is shown in Figure 10. At a lower VED of 69.3 J/mm^3, a shallower melt pool was observed with a more conical morphology. The average width and depth of the melt pool was around 110.22 $\pm$ 8.04 µm and 63.45 $\pm$ 11.19 µm, respectively. The width of the melt pool was similar to the laser beam diameter ($\approx$ 100 µm). As the energy density increased, the melt pool became deeper and had a semi-spherical

morphology. At a VED of 151.5 J/mm^3, the average width and the depth of the melt pool was around 133.70 ± 10.84 µm and 90.95 ± 10. 32 µm, respectively. The variation in melt pool depth with energy density has also been reported in prior studies [44] .

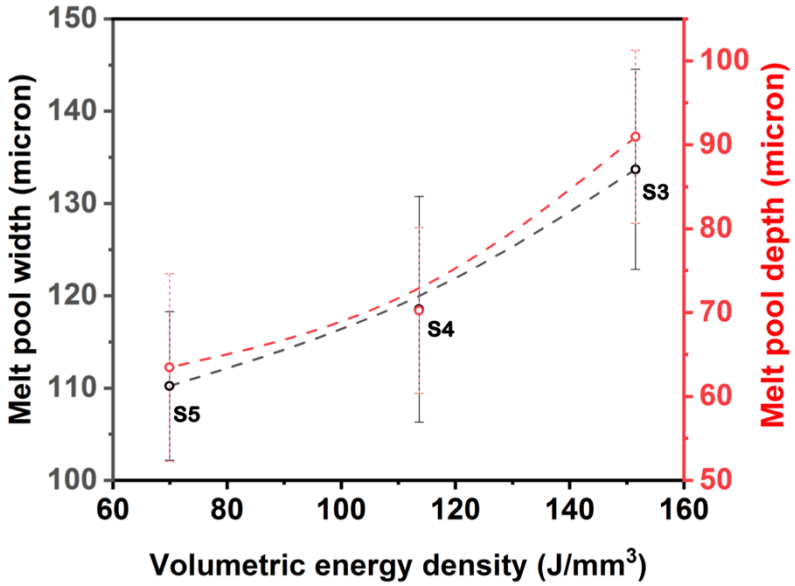

Figure 10 Melt pool width (black) and melt pool depth (red) of the S3, S4, and S5 specimens. A fitted line is used for a visual guide of the two data sets.

3.3 Microstructure maps

3.3.1 Effect of VED on grain morphology and dendrite spacing

PV maps are a convenient way to compare microstructural features as a function of process parameters. The average grain size (Fig. 11a), the grain aspect ratio (Fig. 11b), the average grain boundary misorientation (Fig. 11c), and the primary dendrite arm spacing (Fig. 11d) are summarized as "heat maps" within the acceptable VED boundaries. The average GB misorientation showed similar trends with energy densities as grain size and grain aspect ratio. At lower energy densities, a high fraction of high angle boundary was measured, potentially due to the presence of more spherical grains and higher cooling rates. As the energy density increased, the fraction of high angle boundaries decreased. These specimens also showed a higher fraction of columnar grains (Fig. 7c) with grain aspect ratio up to 5.60.

Collectively, the PV maps microstructural refinement (blue) at lower energy densities, with a corresponding increase in grain boundary misorientation. From this visual summary, it is expected that mechanical strength would increase in the lower VED regime. This dependence will be discussed later.

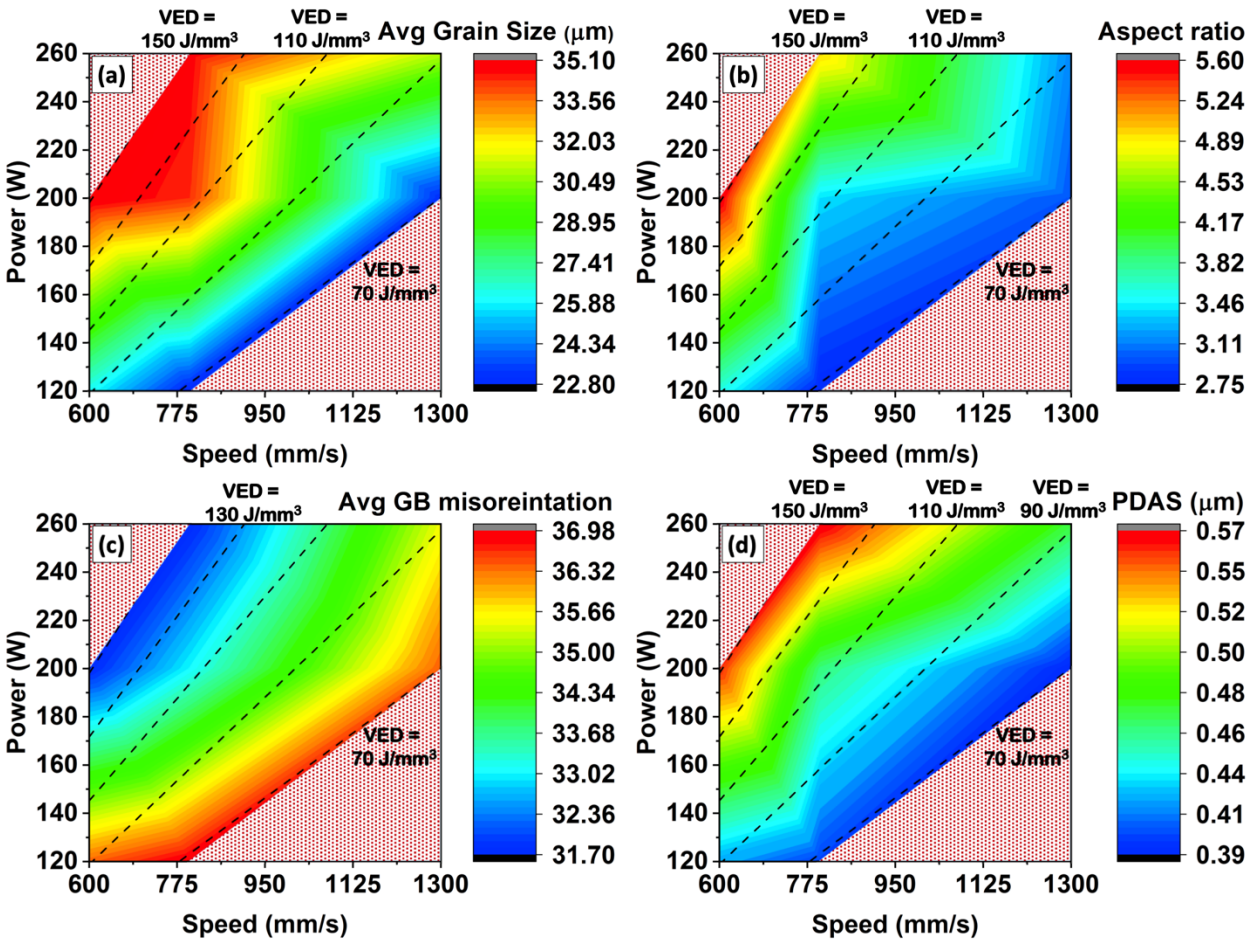

Figure 11 Microstructural mapping of (a) grain size (b) grain aspect ratio and (c) average grain boundary misorientation (d) primary dendrite arm spacing of 316L SS fabricated using SLM techniques. Heat maps are generated using data points of the S1-S7 specimens.

3.3.2 Effect of VED on crystallographic texture

Texture analysis and IPF mapping of the LT specimens are summarized and shown in Figure 12. The specimens with energy densities around 70 J/mm^3 showed a more random texture. As the energy density increased, a texture towards (110) formed. In different alloy systems, similar texture anisotropy results in as-built SLM components were also reported [19,45–47]. A further increase in energy densities (above 110 J/mm^3) resulted in a grain orientation shift towards the (100) plane with respect to the build direction. A stronger (100) texture is expected at very high energy densities (VED > 150 J/mm^3). A (100) texture promotes epitaxial grain growth since it is well aligned with the preferential FCC crystal growth direction [48], supporting the presence of coarser grains, higher grain aspect ratio, and low angle grain boundaries at higher energy densities (Fig 11). A texture variation with energy density can be used to manipulate the mechanical properties of the as-fabricated structures [49].

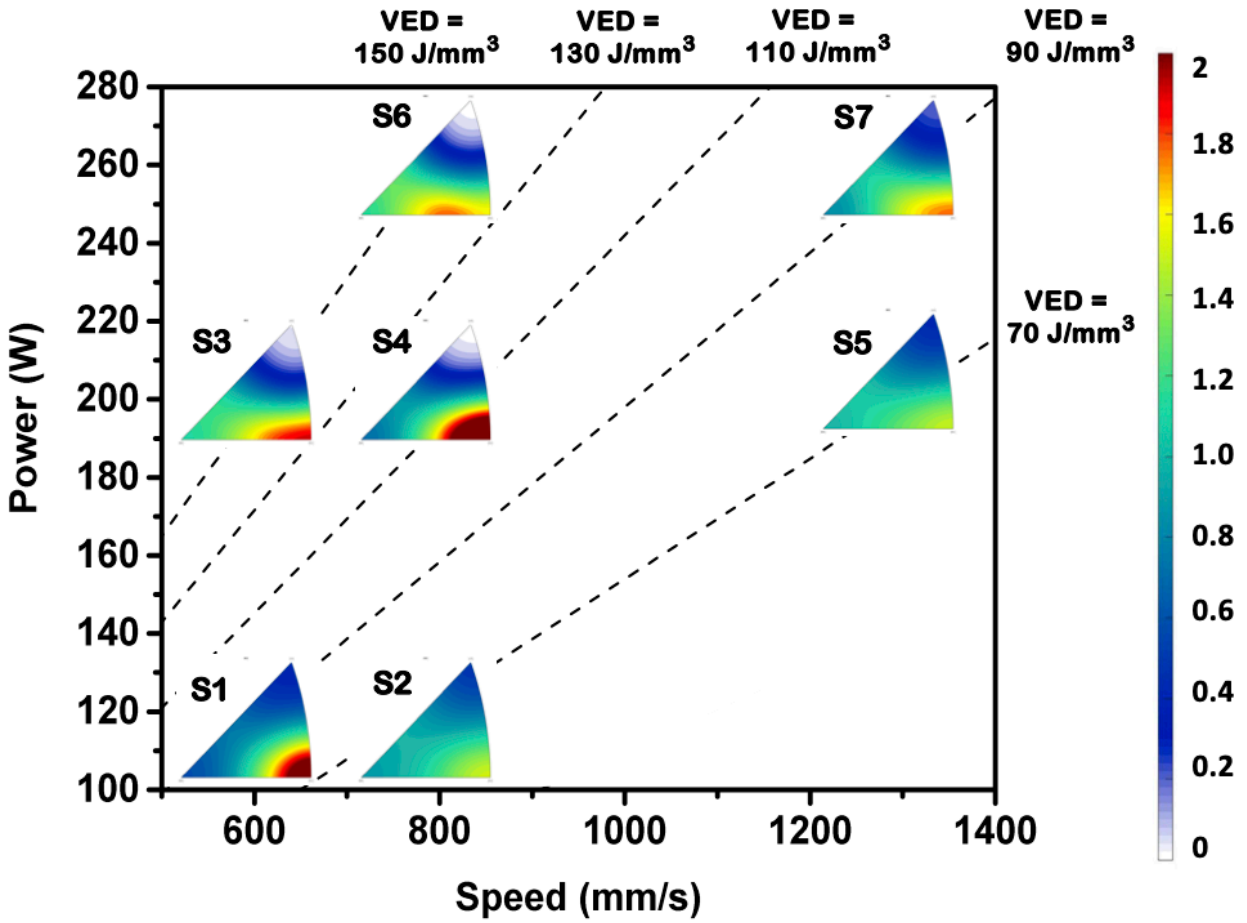

Figure 12 IPF maps of the S1-S7 specimens drawn over the PV map. The reference direction for the IPF maps is the Build direction.

4. DISCUSSION

4.1 High-throughput approach for processing map boundaries

In the experimental design of this study, 200 hex nut specimens, each at different processing parameters, were fabricated in a single batch. These specimens were fabricated over a few initial deposition layers of the porous support structure enabling easy removal using a socket wrench. This study demonstrates that hex nut geometries of similar dimensions are useful for HT investigations.

HT characterization involving immersion-based density measurements and Rockwell hardness measurements was conducted on 425 hex nut specimens. In many cases, these techniques may show marginal deviation from the actual values, but they are effective for quick approximation [41]. For example, the surface roughness of the as-fabricated SLM specimens may introduce errors in both hardness and density measurements. Some other valuable information such as defect's size, morphology, distribution also cannot be traced using these techniques. For such measurements, electron microscopes or x-ray microtomography would be a more suitable technique. However, electron microscopy and microtomography techniques can't be used for HT measurement, as analyzing hundreds of specimens using these techniques would not be feasible. The time estimation for HT fabrication is around 12 hours, out of which most of the time is devoted to the automated printing process. On average, HT immersion-based density measurement takes 2

minutes per specimen, and hardness measurement takes 4 minutes per specimen. As a result, HT fabrication and characterization can be performed within 2-3 days for a batch containing 200 specimens.

4.1.1 VED as a design parameter

In the present study, both density and hardness measurement showed a strong correlation with VED (slope of PV graph) as demonstrated in Fig. 2a and 2b. Prior studies on 316 SS and Al-Si alloys have highlighted the limitations of volumetric energy density [50,51] as it fails to capture the overall melt pool physics. These previous studies have shown different density and hardness values for the same values of VED. In the present study, similar density and hardness values were observed for the specimens with constant energy density, at least at the very coarse level afforded with the HT methods. At and beyond VED boundaries, like VED = 151.5 J/mm^3 where keyholing porosity is predicted, variation in hardness (50.1 to 40.0 HRA) was observed. This suggests that VED can be considered as a reliable parameter, at least within the boundary regions used in this study, but at too high or too low VED, power or velocity independently may have a stronger effect on the microstructure.

4.1.2 Low VED regions

HT characterization allows a rapid description of processing conditions as well as bounding of processing parameters (Fig. 2). The microscopic examination also confirmed the presence of open pores (Fig. 2a) and lack-of-fusion pores (Fig. 3c) in these specimens. The agreement between HT and LT study highlights the reliability of a HT approach in identifying the lower bound of the processing window. To quantify the validity of this approach, existing models were compared. A model proposed by Tang *et al*. [10] was used to compare the experimental and the predicted value of the lack-of-fusion offset. In this model, the criterion for full melting in terms of melt pool geometry was given by:

$$\left(\frac{h}{W}\right)^2 + \left(\frac{t}{D}\right)^2 \leq 1 \qquad \text{(Eq. 4)}$$

Here, W is the melt pool width (mm), D is the melt pool depth (mm), h is hatch spacing (= 0.11 mm), and t is layer thickness (= 0.02 mm). A two-dimensional Rosenthal equation for moving heat source was used to estimate the melt pool shape [10]. Assuming a semi-elliptical melt pool shape (with W=2D), the width of the melt pool was expressed as:

$$W = \sqrt{\frac{8\alpha l_p}{\pi e \rho C v_s (T_m - T_o)}} \qquad \text{(Eq. 5)}$$

where, α is laser absorptivity ($\approx$ 0.6), $l_p$is laser power (W), ρ is the density of the material (8000 kg/m^3), C is specific heat (450 J/KgK), T_m is melting temperature (1723 K), T_o is the far away temperature (298 K), and v_s is scanning speed (m/s). The thermophysical data for the 316L SS was taken from the literature [43]. Combining both equations, the lack-of-fusion offset can be estimated, and the lower processing bound for 316L SS can be written as (in SI units):

$$\frac{l_p}{v_s} = 0.000127 J/m \quad \text{(Eq. 6)}$$

For a constant hatch spacing and layer thickness, the lack-of-fusion offset for 316L SS was estimated to be at a VED = 57.7 J/mm^3. If the laser absorptivity coefficient was taken to be 0.5, the lower bound offset can be estimated to be VED = 69.3 J/mm^3. The value of the laser absorptivity coefficient is hard to precisely measure; thus lack-of-fusion can be estimated to be between 55-70 J/mm^3. The analytical estimate is consistent with the HT measurements.

In addition to the hardness and density trends in the VED plots, the validity of equations 5 and 6 is evident with the melt pool results plotted in Fig. 10. At the lowest energy density (i.e., 70 J/mm^3), the melt pool widths were 110 µm. With a hatch spacing of 110 µm for these LT specimens, the limit for overlap of melt pools has been reached.

4.1.3 High VED regions

A maximum plateau in density and hardness was observed over a range of VED (70-150 J/mm^3) (Fig. 2). Increased scatter, particularly in hardness, was observed above a VED ≈ 150 J/mm^3. To quantify the proposed onset of keyholing, a theoretical model proposed by King *et al.* [52] was used to estimate the keyholing offset. In this model, the transition from the heat conduction mode to the keyholing mode was predicted in terms of normalized enthalpy. The normalized equation as a function of SLM input processing parameters can be expressed as:

$$\frac{\Delta H}{H_s} = \frac{\alpha l_p}{\pi \rho C T_m \sqrt{D v_s r_l^3}} \quad \text{(Eq. 7)}$$

where α is laser absorptivity (≈ 0.6), l_p is laser power (W), ρ is the density of the material (8000 kg/m^3), C is specific heat (840 J/KgK), T_m is melting temperature (1723 K), D is thermal diffusivity (5x10^{-6} m^2/s), v_s is scanning speed (m/s), and r_l is laser spot size (≈ 50 x10^{-6} m). For keyholing to occur, normalized enthalpy ($\Delta H/H_s$) should exceed the value $\pi T_b/T_m \approx 6$, where T_b and T_m are the boiling and the melting point of the alloy. Using the above values, the keyholing threshold for 316L SS can be written as (in SI units):

$$\frac{l_p}{\sqrt{v_s}} = 287.42 \text{ J}(ms)^{-0.5} \quad \text{(Eq. 8)}$$

Based on equation 8, the keyholing threshold was estimated to be around VED = 145-165 J/mm^3. It is important to note that the specimens below the predicted energy densities are essentially free from keyhole defects. While the specimens above this threshold value may or may not have keyhole defects, and the probability of their occurrence will increase with increasing VED. A LT microscopic examination revealed the presence of keyhole type defects at VED = 212.12 J/mm^3 (Fig 3a) correlating well with the theoretical model and the HT density measurements.

Overall, HT experiments are quick, efficient, and reliable in identifying the lower and higher VED bounds of the processing window, and the bounds are consistent with analytical approximations. In addition, the real value of this HT technique lies in creating large datasets that can effectively couple with machine learning models for rapid processing parameter discovery.

Ideally, this approach can be applied to any material system and within a span of 2-3 days, hundreds of specimens can be fabricated, extracted, and analyzed to determine the processing bounds.

4.2 Low-throughput microstructure dependence on the melt pool geometry

Complementing the rapid determination of processing conditions using the HT methodology, LT microstructural investigations can provide useful trends and physical insights, particularly as these features relate to the melt pool. A schematic model based on melt pool geometry is proposed to explain variations in the microstructures of the as-fabricated SLM components (Figure 13). In case 1, the lower VED values leads to a shallower melt pool and faster cooling [53,54]. As a result, grains nucleate and grows from the boundary and the center of the melt pool. Upon solidification, these grains will show an overall finer grain sizes due to the multiple nucleation sites and more random texture due to the random distribution in the grain growth direction. This hypothesis is supported by the data collected at a relatively lower VED of 69.9 J/mm^3 where finer grains, lower grain aspect ratio, and finer dendritic microstructures were observed (Fig. 11). These specimens also showed random texture along with higher average GB misorientations.

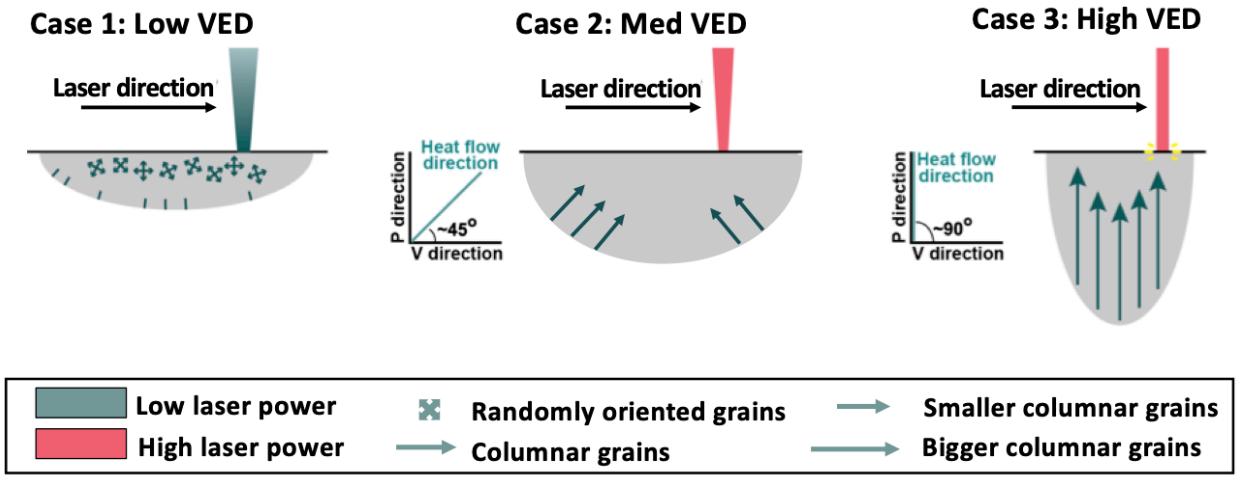

Figure 13 Microstructure dependence on the melt pool geometry of as-fabricated SLM components. At lower VED, spherical grains having random texture forms (represented by the four-headed arrow). With increasing VED, increasing columnar grains form with a texture towards (110) and then (100). The arrows represent columnar grains, and the size of the arrow represents the columnar grain size.

In case 2, medium range VED, a hemispherical melt pool forms coupled with a lower cooling rate than case 1. In this case, grains nucleate only from the melt pool boundaries and grow along the heat flow direction. Upon solidification, these grains will have a relatively coarser grain size. For such melt pool shapes, the heat flow direction would be somewhere around 30-60 degrees with respect to building direction. Since FCC crystals have a preferential growth direction along [100] direction [48] , most of the grains (~45 degrees) will have a (110) orientation along the planar surface. This hypothesis is supported by the experimental data at a VED of 113.6 J/mm^3, where both coarser grains and primary dendrite arm spacings were observed (Fig. 11). These specimens also showed (110) plane crystallographic texture along the build direction.

In case 3 (Fig. 13), the high energy density leads to the formation of a deep melt pool coupled with the lowest cooling rate [53,54]. In this case, grains nucleate from the melt pool boundary and grow along the heat flow direction. Upon solidification, these grains will have the coarsest grain size and the coarsest dendrite arm spacing due to lower cooling rates. Since the laser speed is slower in this scenario, the laser power will have the most influence on the heat flow direction (i.e., (100)). Since FCC crystals grow preferentially along the [100] direction [48], most of the grains show crystallographic texture trending towards the (100) plane. The model presented is supported by experiments at a VED of 151.5 J/mm^3 where the coarsest average grain size of 35.07 μm and a primary dendrite arm spacing of 0.56 μm were observed (Fig. 11). The grain aspect ratio was also 5.60 as compared to 2.75 at lower VED, and there was a higher fraction of low angle grain boundaries. The proposed melt pool model is further supported by the IPF maps (Fig. 12). The crystallographic texture in the build direction started to shift from (110) to (100) plane as the VED increased.

It is evident that the dendrite spacings could be useful in a more systematic study of solidification behavior and cooling rates, and this is being considered for a future study. In addition, stable secondary dendrite arm spacings would provide a more rigorous evaluation of cooling rates.

4.3 Predicting mechanical response as a function of input processing parameters

Microstructure of the as-fabricated specimens can promote change in the hardness and mechanical properties of a material. Common mechanisms to improve the strength of the as-fabricated AM materials include grain boundary strengthening, dislocation sub-structure strengthening, and dislocation density strengthening. Previous studies [4,55] have reported that the cellular dendritic solidification structures have a greater influence on yield strength than the grain size in SLM-fabricated 316L SS. The effective strengthening is primarily due to the presence of dense dislocation networks in the interdendritic regions. The dependence of yield strength on primary dendrite arm spacing is given by the Hall-Petch relationship:

$$\sigma_y = \sigma_o + k_{HP}/\sqrt{PDAS} \qquad \text{(Eq. 9)}$$

where $\sigma_y$is the yield strength (MPa), σ_o is the Peierls stress for dislocation motion (MPa), k_{HP} is Hall-Petch constants (MPa$\sqrt{\mu m}$), and $PDAS$ is primary dendrite arm spacing (μm). For 316L values of σ_o and k_{HP} are 183.31 MPa and 253.66 MPa$\sqrt{\mu m}$, respectively [4].

Table 3. Comparison of the estimated yield strength and the measured hardness value

VED (J/mm^3)	Measured PDAS (μm) (eqn. 3)	Calculated Yield Strength (MPa) (eqn. 9) [4]	Measured Hardness (HRA) (eqn. 2)	% Drop in Yield Strength	% Drop in Hardness
69.1	0.39	589.34	49.51	--	--
90.9	0.43	569.37	48.31	3.39	2.42
113.5	0.47	551.49	47.07	6.42	4.93
149.6	0.54	527.47	45.08	10.54	8.94

Using equations 3 and 9, contributions of the primary dendrite arm spacing to the strengthening were estimated. Similarly, for different VED values, measured hardness values were calculated using equation 2. A comparison of the estimated yield strength and the measured

hardness value is shown in Table 3. With an increase in VED from 70 to 150 J/mm^3 a drop of about 10% was observed in both the hardness and estimated yield strength value. The quick comparison suggest consistency between the measured hardness values (using HT technique) and the contribution of the primary dendrite arm spacing to the estimated yield strength (using LT technique). These results provide the basis for predicting the specimen's hardness and yield strength, solely based on input process parameters for 316L. Further tensile or compressive tests will improve the accuracy of such relationships and will provide better predictions of the mechanical properties. It would also be useful to study the effects of thermal cycles and thermal fatigue on the mechanical response of the as-fabricated components.

5. CONCLUSION

In the present study, a combination of high-throughput and low-throughput investigations were used to understand the influence of processing parameters on the microstructure and properties. Based on the results and analysis, the following conclusions can be reached:

1. The high-throughput approach is a quick, reliable, and effective way for designing processing bounds of as-fabricated SLM components.
    a) A hex nut geometry is useful for high-throughput fabrication, density and hardness measurements.
    b) Quick density and hardness measurements enabled mapping of the lack-of-fusion region and keyholing regions, and both regions were supported with analytical models.
    c) The high-throughput analysis can be completed in a 2-3 day period, allowing rapid definition of process parameters for an alloy system.
2. Energy densities permit microstructural design strategies with low-throughput studies.
    a) At lower energy densities of (VED = 69.9 J/mm^3) finer grains, low grain aspect ratios, finer dendritic structure, and more random texture were observed.
    b) As the energy density increased, coarser grains with higher grain aspect ratios were observed.
    c) Under a constant energy density, the microstructure remained unchanged.
3. The variation in microstructures at different energy densities can be explained in terms of melt pool geometry. Lower energy density results in shallower melt pool and faster cooling rates lead to more randomly oriented, fine grain structures. Higher energy densities result in deeper melt pools and slower cooling rates, leading to coarse elongated grains with a texture towards (110) and (100) planes with respect to the build direction.
4. High-throughput regression of hardness as a function of volumetric energy density (VED) was consistent with a Hall-Petch relationship corresponding to the primary dendrite arm spacings (determined with low-throughput characterization).

CRediT authorship contribution statement:
Ankur Kumar Agrawal: Conceptualization, Methodology, Investigation, Data curation, Formal analysis, Visualization, Writing - original draft, Writing - review & editing. **Gabriel Meric de Bellefon**: Conceptualization, Methodology, Investigation, Writing - review & editing. **Dan Thoma**: Conceptualization, Methodology, Supervision, Resources, Funding acquisition, Project administration, Writing - review & editing.

Declaration of competing interest:

This report was prepared as an account of work sponsored by an agency of the United States Government. Neither the United States Government nor any agency thereof, nor any of their employees, makes any warranty, express or implied, or assumes any legal liability or responsibility for the accuracy, completeness, or usefulness of any information, apparatus, product, or process disclosed, or represents that its use would not infringe privately owned rights. Reference herein to any specific commercial product, process, or service by trade name, trademark, manufacturer, or otherwise does not necessarily constitute or imply its endorsement, recommendation, or favoring by the United States Government or any agency thereof. The views and opinions of authors expressed herein do not necessarily state or reflect those of the United States Government or any agency thereof.

Acknowledgement:

Authors would like to acknowledge partial support by the Department of Energy / National Nuclear Security Administration under Award Number(s) DE-NA0003921. The electron microscopy was carried out using facilities and instrumentation that are partially supported by the National Science Foundation (NSF) through the Materials Research Science and Engineering Center (DMR-1720415). Finally, EBSD training and discussion with Dr. Kaila Bertsch, as well as EOS assistance from Mythili Thevamaran, are greatly appreciated.

REFERENCES

[1] W.E. Frazier, Metal additive manufacturing: A review, J. Mater. Eng. Perform. 23 (2014) 1917–1928.

[2] C.Y. Yap, C.K. Chua, Z.L. Dong, Z.H. Liu, D.Q. Zhang, L.E. Loh, S.L. Sing, Review of selective laser melting: Materials and applications, Appl. Phys. Rev. 2 (2015) 041101.

[3] D. Zhang, S. Sun, D. Qiu, M.A. Gibson, M.S. Dargusch, M. Brandt, M. Qian, M. Easton, Metal Alloys for Fusion-Based Additive Manufacturing, Adv. Eng. Mater. 20 (2018) 1–20.

[4] Y.M. Wang, T. Voisin, J.T. McKeown, J. Ye, N.P. Calta, Z. Li, Z. Zeng, Y. Zhang, W. Chen, T.T. Roehling, R.T. Ott, M.K. Santala, P.J. Depond, M.J. Matthews, A. V. Hamza, T. Zhu, Additively manufactured hierarchical stainless steels with high strength and ductility, Nat. Mater. 17 (2018) 63–70.

[5] M. Seifi, A. Salem, J. Beuth, O. Harrysson, J.J. Lewandowski, Overview of Materials Qualification Needs for Metal Additive Manufacturing, Jom. 68 (2016) 747–764.

[6] T. DebRoy, H.L. Wei, J.S. Zuback, T. Mukherjee, J.W. Elmer, J.O. Milewski, A.M. Beese, A. Wilson-Heid, A. De, W. Zhang, Additive manufacturing of metallic components – Process, structure and properties, Prog. Mater. Sci. 92 (2018) 112–224.

[7] R. Li, J. Liu, Y. Shi, L. Wang, W. Jiang, Balling behavior of stainless steel and nickel powder during selective laser melting process, Int. J. Adv. Manuf. Technol. 59 (2012) 1025–1035.

[8] A.A. Martin, N.P. Calta, S.A. Khairallah, J. Wang, P.J. Depond, A.Y. Fong, V. Thampy, G.M. Guss, A.M. Kiss, K.H. Stone, C.J. Tassone, J. Nelson Weker, M.F. Toney, T. van Buuren, M.J. Matthews, Dynamics of pore formation during laser powder bed fusion additive manufacturing, Nat. Commun. 10 (2019) 1987.

[9] S.A. Khairallah, A.T. Anderson, A.M. Rubenchik, W.E. King, Laser powder-bed fusion additive manufacturing: Physics of complex melt flow and formation mechanisms of pores, spatter, and denudation zones, Addit. Manuf. Handb. Prod. Dev. Def. Ind. 108 (2017) 613–628.

[10] M. Tang, P.C. Pistorius, J.L. Beuth, Prediction of lack-of-fusion porosity for powder bed fusion, Addit. Manuf. 14 (2017) 39–48.

[11] T. Mukherjee, V. Manvatkar, A. De, T. DebRoy, Dimensionless numbers in additive manufacturing, J. Appl. Phys. 121 (2017) 064904.

[12] R. Cunningham, C. Zhao, N. Parab, C. Kantzos, J. Pauza, K. Fezzaa, T. Sun, A.D. Rollett, Keyhole threshold and morphology in laser melting revealed by ultrahigh-speed x-ray imaging, Science (80-.). 363 (2019) 849–852.

[13] H.D. Carlton, A. Haboub, G.F. Gallegos, D.Y. Parkinson, A.A. MacDowell, Damage evolution and failure mechanisms in additively manufactured stainless steel, Mater. Sci. Eng. A. 651 (2016) 406–414.

[14] T.R. Smith, J.D. Sugar, J.M. Schoenung, C. San Marchi, Relationship between manufacturing defects and fatigue properties of additive manufactured austenitic stainless steel, Mater. Sci. Eng. A. 765 (2019) 138268.

[15] W.J. Sames, F.A. List, S. Pannala, R.R. Dehoff, S.S. Babu, The metallurgy and processing science of metal additive manufacturing, Int. Mater. Rev. 61 (2016) 315–360.

[16] U. Scipioni Bertoli, B.E. MacDonald, J.M. Schoenung, Stability of cellular microstructure in laser powder bed fusion of 316L stainless steel, Mater. Sci. Eng. A. 739 (2019) 109–117.

[17] T.R. Smith, J.D. Sugar, C. San Marchi, J.M. Schoenung, Strengthening mechanisms in directed energy deposited austenitic stainless steel, Acta Mater. 164 (2019) 728–740.

[18] L. Liu, Q. Ding, Y. Zhong, J. Zou, J. Wu, Y.-L. Chiu, J. Li, Z. Zhang, Q. Yu, Z. Shen, Dislocation network in additive manufactured steel breaks strength–ductility trade-off, Mater. Today. 21 (2018) 354–361.
[19] O. Andreau, I. Koutiri, P. Peyre, J.-D. Penot, N. Saintier, E. Pessard, T. De Terris, C. Dupuy, T. Baudin, Texture control of 316L parts by modulation of the melt pool morphology in selective laser melting, J. Mater. Process. Technol. 264 (2019) 21–31.
[20] B. Rankouhi, K.M. Bertsch, G. Meric de Bellefon, M. Thevamaran, D.J. Thoma, K. Suresh, Experimental validation and microstructure characterization of topology optimized, additively manufactured SS316L components, Mater. Sci. Eng. A. 776 (2020) 139050.
[21] R. Seede, D. Shoukr, B. Zhang, A. Whitt, S. Gibbons, P. Flater, A. Elwany, R. Arroyave, I. Karaman, An ultra-high strength martensitic steel fabricated using selective laser melting additive manufacturing: Densification, microstructure, and mechanical properties, Acta Mater. 186 (2020) 199–214.
[22] M. Shamsujjoha, S.R. Agnew, J.M. Fitz-Gerald, W.R. Moore, T.A. Newman, High Strength and Ductility of Additively Manufactured 316L Stainless Steel Explained, Metall. Mater. Trans. A Phys. Metall. Mater. Sci. 49 (2018) 3011–3027.
[23] Z. Li, B. He, Q. Guo, Strengthening and hardening mechanisms of additively manufactured stainless steels: The role of cell sizes, Scr. Mater. 177 (2020) 17–21.
[24] M.S. Pham, B. Dovgyy, P.A. Hooper, Twinning induced plasticity in austenitic stainless steel 316L made by additive manufacturing, Mater. Sci. Eng. A. 704 (2017) 102–111.
[25] A. Riemer, S. Leuders, M. Thöne, H.A. Richard, T. Tröster, T. Niendorf, On the fatigue crack growth behavior in 316L stainless steel manufactured by selective laser melting, Eng. Fract. Mech. 120 (2014) 15–25.
[26] Y.J. Yin, J.Q. Sun, J. Guo, X.F. Kan, D.C. Yang, Mechanism of high yield strength and yield ratio of 316 L stainless steel by additive manufacturing, Mater. Sci. Eng. A. 744 (2019) 773–777.
[27] Z. Wang, T.A. Palmer, A.M. Beese, Effect of processing parameters on microstructure and tensile properties of austenitic stainless steel 304L made by directed energy deposition additive manufacturing, Acta Mater. 110 (2016) 226–235.
[28] https://www.eos.info/systems_solutions/software_data-preparation.
[29] I.E. Anderson, E.M.H. White, R. Dehoff, Feedstock powder processing research needs for additive manufacturing development, Curr. Opin. Solid State Mater. Sci. 22 (2018) 8–15.
[30] M.L. Green, C.L. Choi, J.R. Hattrick-Simpers, A.M. Joshi, I. Takeuchi, S.C. Barron, E. Campo, T. Chiang, S. Empedocles, J.M. Gregoire, A.G. Kusne, J. Martin, A. Mehta, K. Persson, Z. Trautt, J. Van Duren, A. Zakutayev, Fulfilling the promise of the materials genome initiative with high-throughput experimental methodologies, Appl. Phys. Rev. 4 (2017) 011105.
[31] J.R. Hattrick-simpers, J.M. Gregoire, A.G. Kusne, Perspective : Composition – structure – property mapping in high-throughput experiments : Turning data into knowledge, 053211 (2017) 053211.
[32] R. Liu, A. Kumar, Z. Chen, A. Agrawal, V. Sundararaghavan, A. Choudhary, A predictive machine learning approach for microstructure optimization and materials design, Sci. Rep. 5 (2015) 1–12.
[33] R. Ramprasad, R. Batra, G. Pilania, A. Mannodi-kanakkithodi, C. Kim, Machine learning in materials informatics : recent applications and prospects, Npj Comput. Mater. (2017) 54.
[34] F. Ren, L. Ward, T. Williams, K.J. Laws, C. Wolverton, J. Hattrick-Simpers, A. Mehta,

Accelerated discovery of metallic glasses through iteration of machine learning and high-throughput experiments, Sci. Adv. 4 (2018) 1566.
[35] N.M. Heckman, T.A. Ivanoff, A.M. Roach, B.H. Jared, D.J. Tung, H.J. Brown-Shaklee, T. Huber, D.J. Saiz, J.R. Koepke, J.M. Rodelas, J.D. Madison, B.C. Salzbrenner, L.P. Swiler, R.E. Jones, B.L. Boyce, Automated high-throughput tensile testing reveals stochastic process parameter sensitivity, Mater. Sci. Eng. A. 772 (2020) 138632.
[36] B.C. Salzbrenner, J.M. Rodelas, J.D. Madison, B.H. Jared, L.P. Swiler, Y.L. Shen, B.L. Boyce, High-throughput stochastic tensile performance of additively manufactured stainless steel, J. Mater. Process. Technol. 241 (2017) 1–12.
[37] R. Jafari-Marandi, M. Khanzadeh, W. Tian, B. Smith, L. Bian, From in-situ monitoring toward high-throughput process control: cost-driven decision-making framework for laser-based additive manufacturing, J. Manuf. Syst. 51 (2019) 29–41.
[38] D.R. Clymer, J. Cagan, J. Beuth, Power–Velocity Process Design Charts for Powder Bed Additive Manufacturing, J. Mech. Des. 139 (2017) 100907.
[39] M. Thomas, G.J. Baxter, I. Todd, Normalised model-based processing diagrams for additive layer manufacture of engineering alloys, Acta Mater. 108 (2016) 26–35.
[40] L. Johnson, M. Mahmoudi, B. Zhang, R. Seede, J.T. Maier, H.J. Maier, I. Karaman, A. Elwany, Assessing Printability Maps in Additive Manufacturing of Metal Alloys, Acta Mater. 176 (2019) 1–25.
[41] S.W. Hughes, Archimedes revisited: A faster, better, cheaper method of accurately measuring the volume of small objects, Phys. Educ. 40 (2005) 468–474.
[42] ASTM International, Standard Test Methods for Density of Compacted or Sintered Powder Metallurgy (PM) Products Using Archimedes' Principle, Astm B962-13. i (2013) 1–7.
[43] K.C. Mills, Recommended Values of Thermophysical Properties for Selected Commercial Alloys, 2002.
[44] A.M. Rubenchik, W.E. King, S.S. Wu, Scaling laws for the additive manufacturing, J. Mater. Process. Technol. 257 (2018) 234–243.
[45] V. Livescu, C.M. Knapp, G.T. Gray, R.M. Martinez, B.M. Morrow, B.G. Ndefru, Additively manufactured tantalum microstructures, Materialia. 1 (2018) 15–24.
[46] M. Calandri, S. Yin, B. Aldwell, F. Calignano, R. Lupoi, D. Ugues, Texture and microstructural features at different length scales in Inconel 718 produced by selective laser melting, Materials, 12 (2019) 1293.
[47] L.L. Parimi, G. Ravi, D. Clark, M.M. Attallah, Microstructural and texture development in direct laser fabricated IN718, Mater. Charact. 89 (2014) 102–111.
[48] W. Kurz, Solidification microstructure-processing maps: Theory and application, Adv. Eng. Mater. 3 (2001) 443–452.
[49] E. Strumza, O. Yeheskel, S. Hayun, The effect of texture on the anisotropy of thermophysical properties of additively manufactured AlSi10Mg, Addit. Manuf. 29 (2019) 100762.
[50] U. Scipioni Bertoli, A.J. Wolfer, M.J. Matthews, J.P.R. Delplanque, J.M. Schoenung, On the limitations of Volumetric Energy Density as a design parameter for Selective Laser Melting, Mater. Des. 113 (2017) 331–340.
[51] K.G. Prashanth, S. Scudino, T. Maity, J. Das, J. Eckert, Is the energy density a reliable parameter for materials synthesis by selective laser melting?, Mater. Res. Lett. 5 (2017) 386–390.
[52] W.E. King, H.D. Barth, V.M. Castillo, G.F. Gallegos, J.W. Gibbs, D.E. Hahn, C. Kamath,

A.M. Rubenchik, Observation of keyhole-mode laser melting in laser powder-bed fusion additive manufacturing, J. Mater. Process. Technol. 214 (2014) 2915–2925.
[53] C. Zhao, K. Fezzaa, R.W. Cunningham, H. Wen, F. De Carlo, L. Chen, A.D. Rollett, T. Sun, Real-time monitoring of laser powder bed fusion process using high-speed X-ray imaging and diffraction, Sci. Rep. 7 (2017) 1–11.
[54] V. Manvatkar, A. De, T. DebRoy, Spatial variation of melt pool geometry, peak temperature and solidification parameters during laser assisted additive manufacturing process, Mater. Sci. Technol. (United Kingdom). 31 (2015) 924–930.
[55] Z. Li, T. Voisin, J.T. McKeown, J. Ye, T. Braun, C. Kamath, W.E. King, Y.M. Wang, Tensile properties, strain rate sensitivity, and activation volume of additively manufactured 316L stainless steels, Int. J. Plast. 120 (2019) 395–410.